Simultaneous characterization of tumor cellularity and the Warburg effect with PET, MRI and hyperpolarized ^{13}C-MRSI

Christian Hundshammer[1,2,8*₸], Miriam Braeuer[1₸], Christoph A. Müller[3,4,5₸], Adam E. Hansen[6], Mathias Schillmaier[7], Stephan Düwel[1,2,8], Benedikt Feuerecker[1], Steffen J. Glaser[2], Axel Haase[8], Wilko Weichert[4,9], Katja Steiger[9,10], Jorge Cabello[1], Franz Schilling[1], Jan-Bernd Hövener[11]; Andreas Kjær[6], Stephan G. Nekolla[1], Markus Schwaiger[1]

[1]Department of Nuclear Medicine, Klinikum rechts der Isar, Technical University of Munich, 81675 München, Germany

[2]Department of Chemistry, Technical University of Munich, 85748 Garching, Germany

[3]Department of Radiology, Medical Physics, University Medical Center Freiburg, Faculty of Medicine, University of Freiburg, 79106 Freiburg, Germany

[4]German Consortium for Cancer Research (DKTK), 69120 Heidelberg, Germany

[5]German Cancer Research Center (DKFZ), 69120 Heidelberg, Germany

[6]Department of Clinical Physiology, Nuclear Medicine & PET and Cluster for Molecular Imaging Rigshospitalet and University of Copenhagen, 2100 Copenhagen, Denmark

[7]Department of Radiology, Klinikum rechts der Isar, Technical University of Munich, 81675 München, Germany

[8]Munich School of Bioengineering, Technical University of Munich, 85748 Garching, Germany

[9]Department of Pathology, Klinikum rechts der Isar, Technical University Munich, 81675 München, Germany

[10]Comparative Experimental Pathology, Klinikum rechts der Isar, Technical University Munich, 81675 München, Germany

[11]Section for Biomedical Imaging, Molecular Imaging North Competence Center (MOINCC), Department for Radiology and Neuroradiology, University Medical Center Kiel, University Kiel

₸equal author contribution

Table of Contents

Supplementary Tables

S1 ^{1}H-MRI acquisition parameters

Table S1. Acquisition parameters of ^{1}H-MRI sequences

	Dim.	slice thickn. / mm	FOV / mm^2	*TR* / ms	*TE* / ms	Matrix	nom. resol. / mm^3	avg.	Slices / slab	AQ time
MRAC UTE	3	1.6	300×300	11.94	0.07	-	4.1	-	192	2min 2s
T_1 MPRAGE	3	1	250×211	1120	3.02	256×256	0.8	4	60	16 min
T_2 FLAIR	3	1	250×211	5000	91	256×256	0.8	2.7	60	6min 4s
T_1 Flash	2	3	160×160	250	2.48	320×320	0.75	2	-	2min 9s
T_2 HASTE	2	3	160×160	1600	93	256×256	1.2	20	-	1min 33s
Diffusion[a]	2	3	70×70	4000	71	48×48	6.4	8	-	6min 55s

[a] *b*-values: 10, 150, 300, 500, 700 s*mm^{-2}

AQ time: acquisition time; avg.: averages; Dim.: Dimensions; FLAIR: fluid-attenuated inversion recovery; FLASH: fast low-angle shot; FOV: field of view; HASTE: half Fourier acquisition single shot turbo spin echo; MRAC: magnetic resonance-based attenuation correction; MPRAGE: magnetization prepared rapid acquisition gradient echo; nom. resol.: nominal resolution; T_1: spin lattice relaxation time; T_2: spin spin relaxation time; *TE*: echo time; thickn.: thickness; *TR*: repetition time; UTE: ultra-short echo time.

S2 Pearson correlation of metabolic data measured in tumors of similar cellularity

Table S2. Pearson correlation coefficients for [^{18}F]FDG PET, [1-^{13}C]pyruvate CSI, DWI of tumors with similar cellularity (*ADC* of (0.57±0.04)*10^{-3} mm^{2}s^{-1})

	SUV_{mean}	SUV_{max}	K_i	*MRGlu*	k_{pl}	$k_{pl,\ slice}$	*AUC ratio*	$AUC\ ratio_{slice}$
SUV_{mean}	1							
SUV_{max}	0.98^{****}	1						
K_i	0.65^{*}	0.56^{*}	1					
MRGlu	0.56^{*}	$0.53^{n.s.}$	0.76**	1				
k_{pl}	0.59^{*}	$0.51^{n.s.}$	0.57^{*}	$0.05^{n.s.}$	1			
$k_{pl,\ slice}$	0.56^{*}	$0.46^{n.s.}$	0.65^{*}	$0.26^{n.s.}$	0.70^{**}	1		
AUC ratio	0.59^{*}	0.55*.	0.68^{*}	$0.36^{n.s.}$	0.77^{**}	0.74^{**}	1	
$AUC\ ratio_{slice}$	$0.47^{n.s.}$	$0.45^{n.s}$	0.70^{**}	0.81^{***}	$0.26^{n.s.}$	$0.34^{n.s.}$	0.59^{*}	1

*p < 0.05, **p < 0.01, ***p < 0.001, ****p < 0.0001.

AUC ratio: areas under the curve ratio from tumor region-of-interest ^{13}C-analysis; *AUC* ratio$_{slice}$: areas under the curve ratio from slice-selective like ^{13}C-analysis; K_i: composite rate constant; k_{pl}: pyruvate-to-lactate exchange rate; $k_{pl,\ slice}$: pyruvate-to-lactate exchange rate *from slice-selective like analysis; MRGlu*: metabolic rate of glucose utilization; n.s.: not significant; SUV_{max}: maximum standard uptake value; SUV_{mean}: mean standard uptake value.

S3 Pearson correlation coefficients of ^{13}C-data from slice selective like analysis correlated with longitudinal PET and MRI data

Table S3. Pearson correlation coefficients for of ^{13}C-data from slice selective like analysis correlated with longitudinal PET and MRI data.

	SUV_{mean}	SUV_{max}	K_i	$MRGlu$	$k_{pl, slice}$	AUC_{slice}	d_{t-v}	TMV	TLG	ADC	c_{lac}	c_{glc}
SUV_{mean}	1											
SUV_{max}	0.99^{****}	1										
K_i	0.68^{***}	0.60^{**}	1									
$MRGlu$	0.65^{***}	0.58^{**}	0.94^{****}	1								
$k_{pl, slice}$	$0.39^{\text{n.s.}}$	$0.34^{\text{n.s.}}$	0.41^{*}	$0.14^{\text{n.s.}}$	1							
AUC_{slice}	$0.28^{\text{n.s.}}$	$0.23^{\text{n.s.}}$	$0.31^{\text{n.s.}}$	0.43^{*}	$0.29^{\text{n.s.}}$	1						
d_{t-v}	$0.25^{\text{n.s.}}$	$0.19^{\text{n.s.}}$	$0.45^{*.}$	$-0.07^{.\text{n.s.}}$	0.59^{**}	$0.23^{\text{n.s.}}$	1					
TMV	-0.49^{*}	-0.49*	$-0.37^{\text{n.s}}$	$-0.34^{\text{n.s.}}$	$0.06^{\text{n.s.}}$	$0.23^{\text{n.s.}}$	$0.22^{\text{n.s.}}$	1				
TLG	$-0.29^{\text{n.s.}}$	$-0.29^{\text{n.s.}}$	$-0.27^{\text{n.s.}}$	$-0.24^{\text{n.s.}}$	$0.12^{\text{n.s.}}$	$0.33^{\text{n.s.}}$	$0.26^{\text{n.s.}}$	0.95^{****}	1			
ADC	-0.45^{*}	-0.46*	$-0.36^{\text{n.s}}$	$-0.37^{\text{n.s.}}$	$0.15^{\text{n.s.}}$	$0.35^{\text{n.s.}}$	$0.38^{\text{n.s.}}$	0.81^{****}	0.73^{****}	1		
c_{lac}	-0.52^{**}	-0.48*	$-0.30^{\text{n.s.}}$	$-0.19^{\text{n.s.}}$	$0.04^{\text{n.s.}}$	$-0{,}05^{\text{n.s.}}$	$0.08^{\text{n.s.}}$	0.60^{**}	0.51^{*}	$0.35^{\text{n.s.}}$	1	
c_{glc}	$0.14^{\text{n.s}}$	$0.13^{\text{n.s.}}$	$0.17^{\text{n.s.}}$	0.49^{**}	$-0{,}09^{\text{n.s.}}$	0.41*	$-0.20^{\text{n.s.}}$	$0.02^{\text{n.s.}}$	$0.06^{\text{n.s.}}$	$-0.11^{\text{n.s.}}$	$0.17^{\text{n.s.}}$	1

*p < 0.05, **p < 0.01, ***p < 0.001, ****p < 0.0001.

ADC: apparent diffusion coefficient; *AUC* rat: areas under the curve ratio from tumor region-of-interest ^{13}C-analysis; c_{glc},: blood glucose concentration; c_{lac}: blood lactate concentration; d_{t-v}: distance of tumor to central blood vessel; K_i: composite rate constant; $k_{pl\ slice}$: pyruvate-to-lactate exchange rate from slice-selective like analysis; *MRGlu*: metabolic rate of glucose utilization; n.s.: not significant; SUV_{max}: maximum standard uptake value; SUV_{mean}: mean standard uptake value; *TLG*: total lesion glycolysis, *TMW*: tumor metabolic volume.

Supplementary information and figures

S1 Tumor growth curve

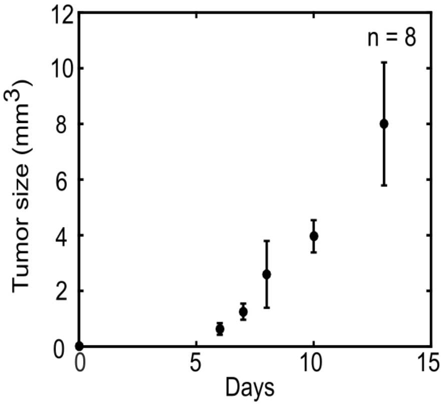

Figure S1. Tumor growth curves of subcutaneous MAT-B-III tumors (n=8).

S2 [^{18}F]FDG PET, input functions and tumor uptake curves

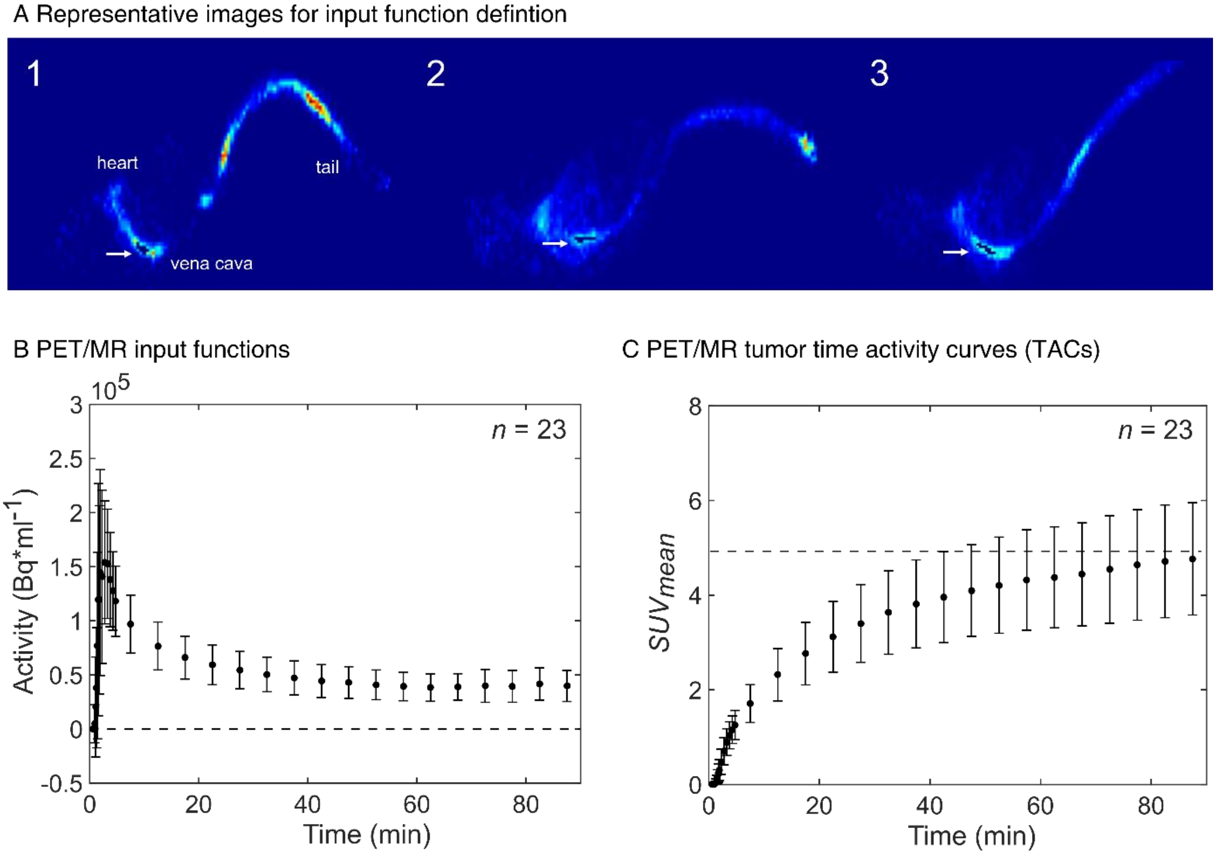

Figure S2. PET/MR input functions and time activity curves of tumors. **(A)** shows three representative coronal images where image derived input functions were segmented semi-automatically. **(B)** shows the mean ± *std* of all image derived input functions except for one animal. An explanation for excluding the animal is given in **Figure S3C4**. **(C)** is the mean ± *std* of all tumor time activity curves corrected by the respective animal weights and injected doses. The measurement of the same animal as mentioned in (B) was excluded.

Image derived input functions (IDIFs) were segmented in the inferior vena cava [1] for kinetic Patlak [2, 3] analysis of the glucose utilization of subcutaneous MAT-B-III tumors. Three exemplary coronal images showing the segmented IDIF ROIs are displayed in **Figure S3A**. Except for one measurement, the mean ± *std* of all measured IDIFs and tumor time activity curves are displayed in **Figure S3B** and **C**, respectively. An explanation for excluding one measurement is given in the next section.

S3 [^{18}F]FDG PET, Patlak analysis

The kinetic Patlak analysis was performed according to equation 1 [2, 3]

$$\frac{c_{tissue}(t)}{c_{plasma}(t)} = K\frac{\int_0^{\tau} c_{plasma}(\tau)d\tau}{c_{plasma}(t)} + V \qquad (1)$$

with t being the time after tracer injection, $c_{tissue}(t)$ being the FDG activity concentration in the tumor, $c_{plasma}(t)$ being the FDG activity concentration in the vena cava (IDIF), ${}_0\int^{\tau} c_{plasma}(\tau)\mathrm{d}\tau$ being the integral of FDG concentration in the vena cava (IDIF), K_i being the composite rate constant ($K_1 \times k_3/(k_2+k_3)$) and V being the FDG distribution volume in the vena cava (IDIF).
A comparison of [^{18}F]FDG tumor uptake curves measured for three animals at a small animal PET/CT scanner and at a clinical PET/MR scanner showed no significant differences. However, the K_i value was by a factor of $f = 2.7$ higher for PET/MR data compared to PET/CT data. A reduced resolution of the PET/MR leads to an underestimation of ${}_0\int^{\tau} c_{plasma}(\tau)\mathrm{d}\tau$ determining higher K_i values (**Figure S3A** and **B**). All PET/MR K_i values (and *MRGlu*) obtained in the longitudinal study were finally corrected by the factor *f*.
Figure S3C1 and **C2** show representative Patlak plots. In some few animals, we noticed that the injection of pyruvate slightly disturbed FDG uptake as shown in (**Figure S3C3**) indicated with a black arrow. We assume that this was due to temporary FDG clearance in the blood stream surrounding the tumor. For one animal, 49.5% FDG resided in the tail vein at first injection but was added to the blood system at pyruvate injection (**Figure S3C4**, indicated with a black arrow). However, the linearity of the Patlak plot in the defined fit range (10 min to 40 min) was still given as this analysis is not dependent on the amount of injected FDG. For an accurate SUV_{mean} and SUV_{max} analysis, the tumor time activity curves of the “first” and the “second” FDG injection were fitted to an exponential function ($y=a\times(1-e^{(-b\times t)})$) and plateau values were extracted. The actual dose of the first injection was calculated according to the ratio of these plateau values.

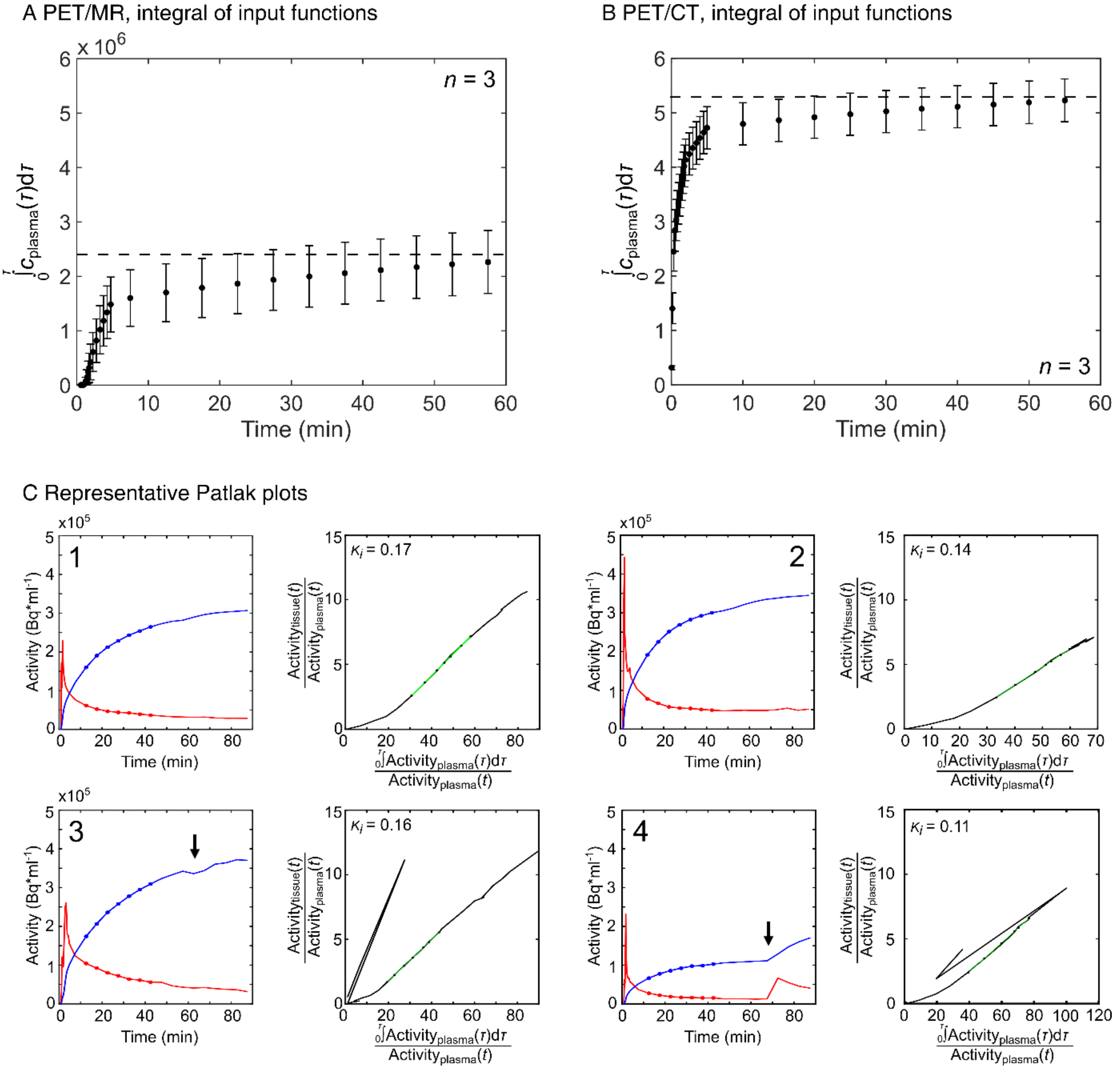

Figure S3. Input function integrals of PET/CT and PET/MR and PET/MR Patlak analysis. **(A)** and **(B)** compare the integrals of the image derived input functions segmented in the vena cava inferior of three animals measured with a delay of about ten hours respectively at the PET/MR and the PET/CT. **(C)** displays four individual image derived input functions and tumor uptake curves in one plot (C1-4). The respective Patlak plots are given to the right of the uptake curves. C1, C2 show good linearity in the chosen time range of 10-40 minutes (green line). In few animals, we observed slight disturbance of tumor FDG uptake at ^{13}C-pryuvate injection (C3, black arrow). For one animal, a major portion of FDG resided in the tail vein at injection but was co-injected at ^{13}C-pyruvate injection (C4). The actual amount of injected FDG was corrected to accurately determine SUV_{mean} and SUV_{max}. Note that the K_i values displayed in the plot C1-4 have not been corrected by f = 2.7.

S4 ^{13}C B_1-calibration and field profile of a ^{1}H/^{13}C surface coil

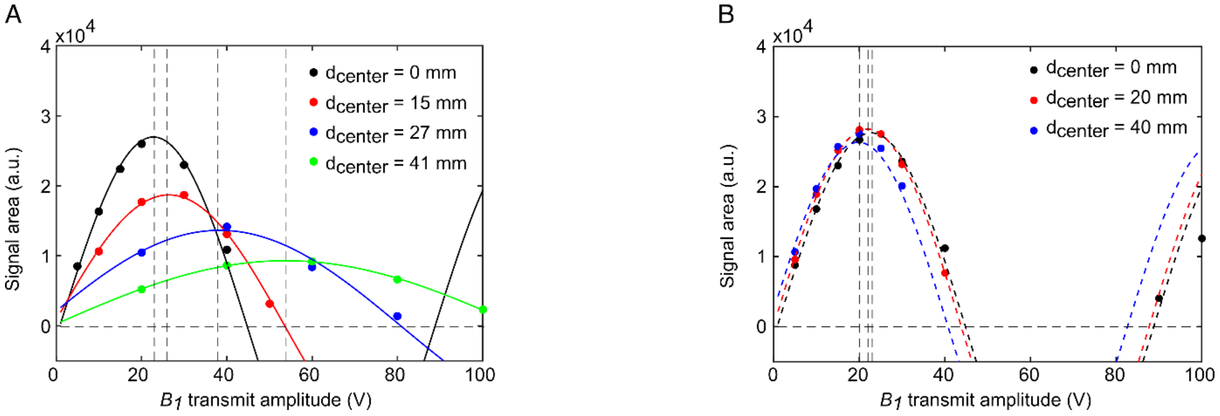

Figure S4. ^{13}C MR signal (dots) and fit (line) of 8 M ^{13}C-urea model solution in a 5 mL glass vial measured as function of transmitter voltage in vertical (A) and horizontal (B) distance to the ^{1}H/^{13}C surface transmit-receive coil. (A) At 35 mm vertical distance, the maximum signal amplitude was decreased by 50% compared to the maximum signal when the phantom was directly placed on the surface of the coil (black). (B) No relevant difference of the MR signal was observed when the position of the model solution was moved by 0-40 mm in horizontal direction (zero vertical direction). These results indicate that the excitation of the CSI sequences is constant in horizontal direction but varies significantly in vertical direction over the examined animals. Tumors were therefore placed directly onto the surface coil (animal position: head first, right lateral) minimizing quantification errors due to B_1 inhomogeneity in vertical direction.

S5 Diffusion-weighted imaging

Reproducibility and validation experiments

We used an ice-water phantom to validate quantitative DWI measurements and verify reproducibility. The phantom consisted of two plastic tubes with the space between the inner and the outer tube being filled with frozen water [4]. The inner tube was filled with water that was kept at a temperature of 0 °C. The setup provides the chance to measure *ADC* values at a constant temperature over a reasonable period of time.

Diffusion-weighted imaging was performed on the clinical 3 T PET/MR scanner (mMR biograph, Siemens, Erlangen, Germany) and on a 7 T preclinical scanner (Avance III, Bruker BioSpin, Billerica, MA, USA). Acquisition parameters at the clinical system were: *TE*/*TR* 74/6000 ms, b-values 10, 150, 300, 500, 700 s/mm², matrix 48×48, FOV 58×58 mm, slice thickness 3 mm, averages 8. Acquisition parameters at the pre-clinical system were: *TE*/*TR* 17/1500 ms, b-values 18, 158, 308, 508, 708 s/mm², matrix 128×128, FOV 40×40 mm, slice thickness 2 mm, averages 3. For the clinical and pre-clinical systems we respectively obtained *ADC* values of 1.105×10^{-3} mm²/s (95% confidence interval: $1.102 – 1.109\times10^{-3}$ mm²/s) and 1.117×10^{-3} mm²/s (95% confidence interval: $1.107 – 1.126\times10^{-3}$ mm²/s), which are in agreement with literature values 1.099×10^{-3} – 1.138 mm²/s (for T = 0-1 °C) [5].

Exemplary T_2-weighted, diffusion-weighted images and *ADC* plots

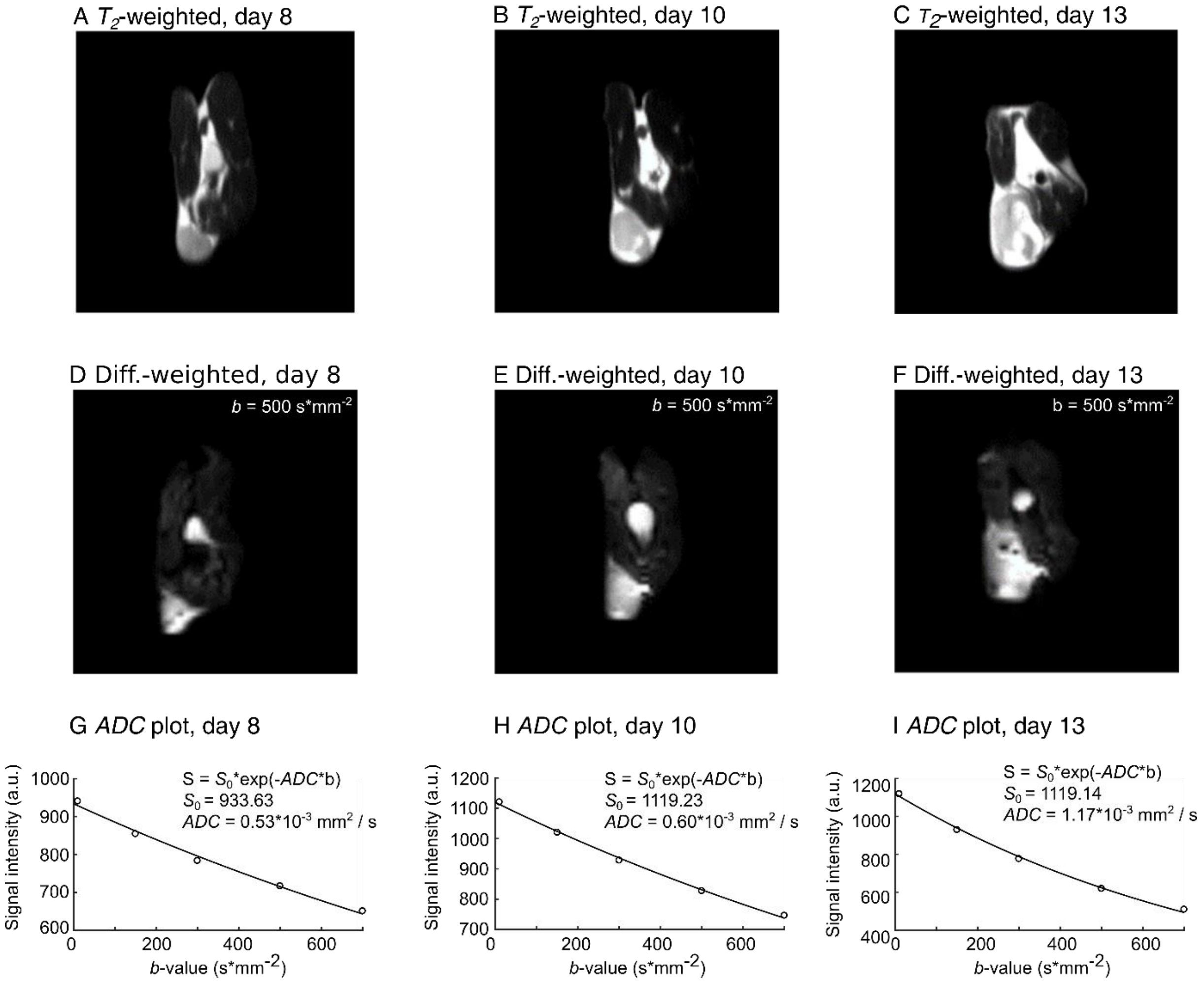

Figure S5. Exemplary T_2-weighted images, diffusion-weighted images and *ADC* fits. (A-C) T_2-weighted images of an animal measured on day eight, ten and thirteen respectively. **(D-F)** Representative diffusion-weighted images acquired for the same animal as in (A-C) for *b*-value = 500 s×mm^{-2}. **(G-I)** Respective *ADC* fits for whole tumor ROIs.

S6 Histology

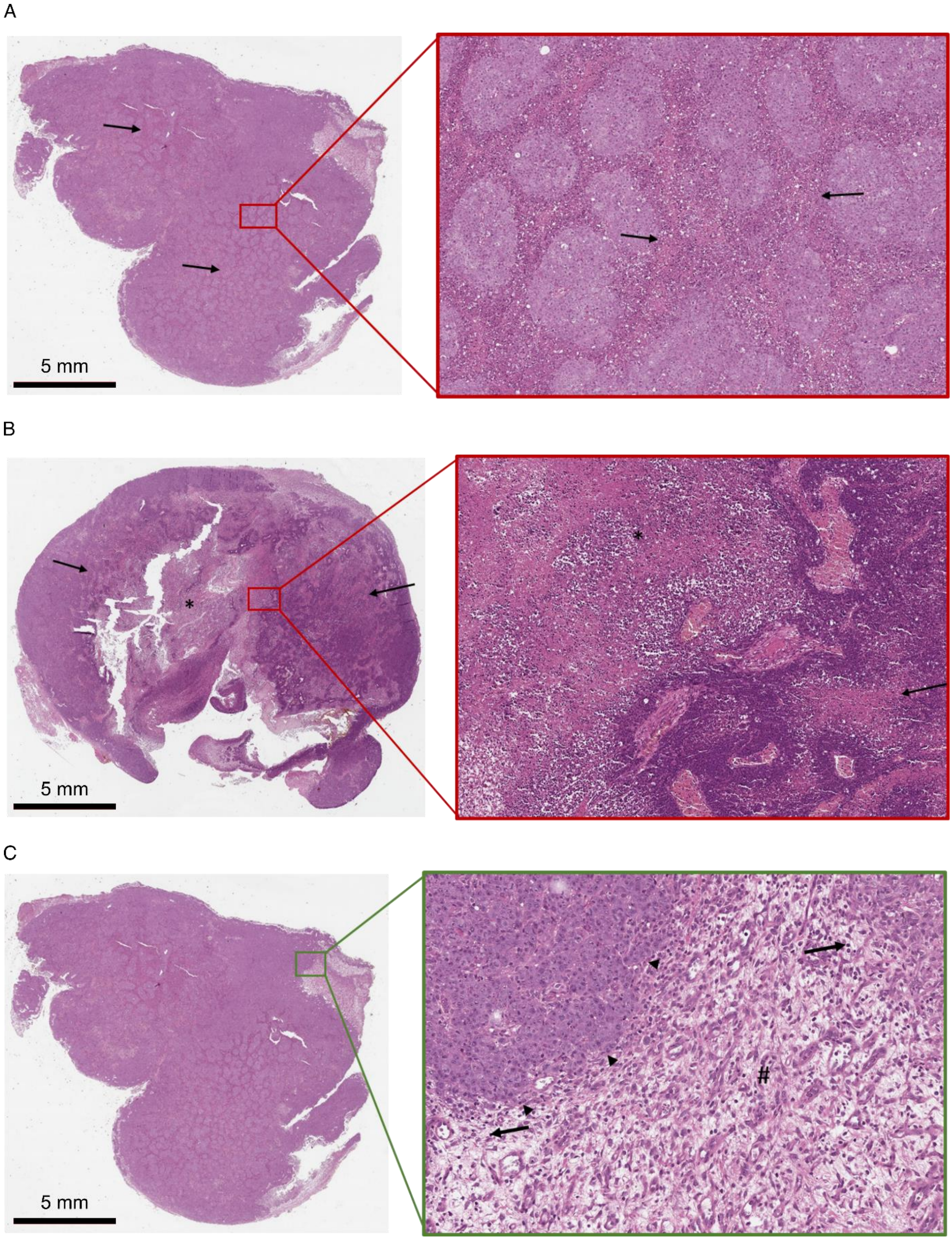

Figure S6. Representative Hematoxylin-Eosin (H.-E.) stained histological tumor slices. (A) tumor slice with a total 15% of tumor area covered by necrosis. The multifocal necrotic parts of the tumors (arrows) in two of the cases did not merge to a large central necrotic area. (H.-E. staining, overview (left), original magnification 100 × (right)). **(B)** tumor slice with a total 35% of tumor area covered by necrosis. The multifocal necrotic parts of the tumors (arrows) in the majority of cases was confluent in a larger central necrosis (*). (H.-E. staining, overview (left), original magnification 100 × (right)). **(C)** example of fibroangioblastic granulation tissue (#) and slight infiltration (lymphocytes, arrows) in tumor (arrowheads) periphery. (H.-E. staining, overview (left), original magnification 200 × (right)).

S7 Correlation plots of %-necrosis with DWI, PET and MRSI data

For validation of signal averaging effects with progressive necrosis in growing tumors, quantitative parameters obtained from DWI, PET and MRSI from n = 7 (out of eight) terminal measurements were correlated with the percentage of necrosis in histological tumor slices

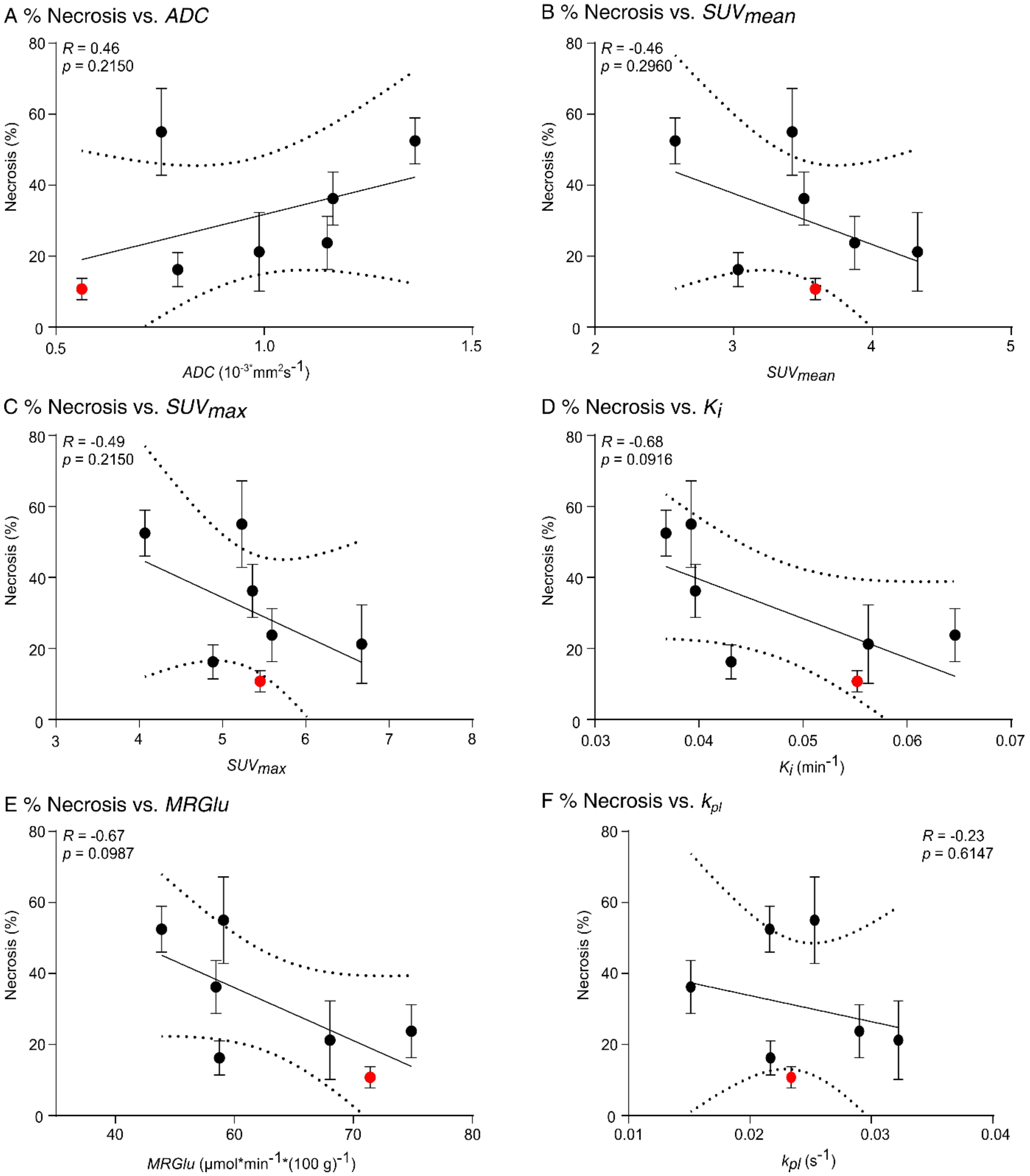

Figure S7. Correlation plots of necrosis and DWI, PET, MRSI data. Correlation of%-necrosis ± standard deviation with **(A)** *ADC*, **(B)** SUV_{mean}, **(C)** SUV_{max}, **(D)** K_i, **(E)** *MRGlu* and **(F)** k_{pl}. Data from the animal sacrificed on day ten are marked in red. Best fit (solid line) and 95% confidence bands (dashed lines). Correlation coefficients for%-necrosis and AUC ratios were: R = -0.21, p = 0.6506.

stained with H.-E. One animal was left out for analysis, because the PET scan failed as described in the materials and methods section in the main manuscript. One animal was sacrificed on day ten, six on day thirteen. Necrosis was estimated for four slices per tumor and the given value is the mean (± standard deviation) for the respective four slices. Overall, the following trend is observed: progressive or bigger tumors showed a higher percentage of necrosis (%-Nec), which was measured by DWI with increasing *ADC* values. %-Nec and *ADC* exhibited a positive correlation (**Figure S7 A**). This led to partial volume artifacts for metabolic data shown by negative correlations with%-Nec (**Figure S7 B-E**). However, correlations were not significant, which was probably due to the small group size and the low spatial correlation of histological slices and MRI/PET/MRSI regions of interest. Note, that only a very weak trend is shown for ^{13}C-MRSI data (**Figure S7 F**).

S8 Quantitative longitudinal data for three groups of similar tumor cellularity each

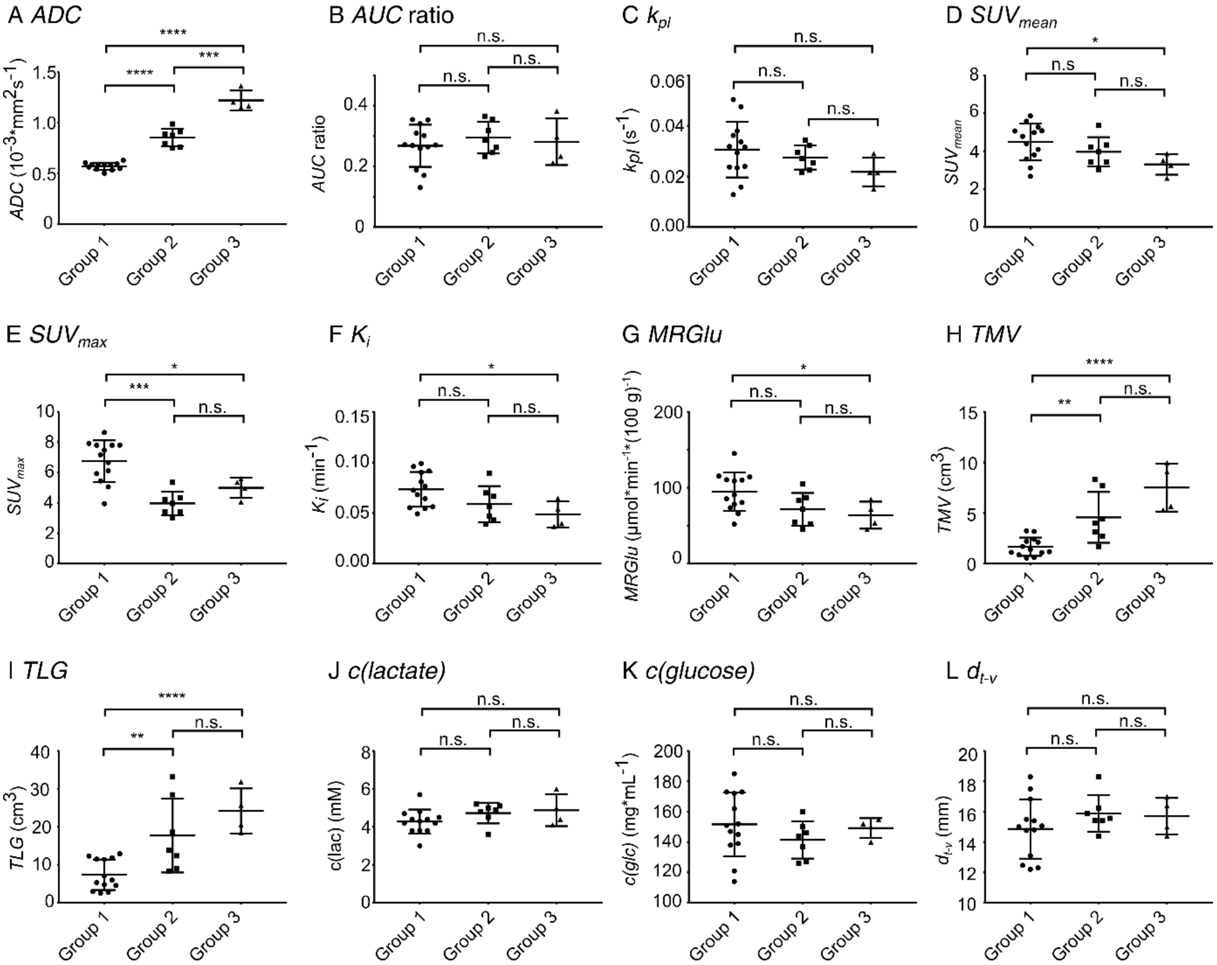

Figure S8. Overview of all multimodal semi-/quantitative longitudinal data measured for animals clustered into three groups of different tumor cellularity (*ADC* values) measured with DWI. (A) *ADC*, **(B)** *AUC* ratios from ^{13}C-MRSI, **(C)** k_{pl} from ^{13}C-MRSI, **(D)** SUV_{mean} from FDG-PET, **(E)** SUV_{max} from FDG-PET,

(F) K_i from FDG-PET, **(G)** *MRGlu* from FDG-PET, **(H)** tumor metabolic volume (*TMV*), **(I)** total lesion glycolysis (*TLG*), **(J)** blood lactate concentration, **(K)** blood glucose concentration, **(L)** distance of tumor to central blood vessel.

Abbreviations

ADC: apparent diffusion coefficient; AQ: acquisition; *AUC* ratio: areas under the curve ratio from tumor region-of-interest ^{13}C-analysis; *AUC* $\text{ratio}_{\text{slice}}$: areas under the curve ratio from slice-selective like ^{13}C-analysis; B_1: radiofrequency excitation field; *b*-value: diffusion-weighting factor; c_{glc}: blood glucose concentration; c_{lac}: blood lactate concentration; $c_{plasma}(t)$: tracer plasma concentration; CSI: chemical shift imaging; CT: computed tomography; $c_{tissue}(t)$: tracer tissue concentration; $d_{t\text{-}v}$: distance between the vena cava and the center of mass of the tumors; DWI: diffusion-weighted imaging; [^{18}F]FDG: 2-deoxy-2-[F^{18}]fluoro-D-glucose; FLASH: fast low-angle shot; FLAIR: fluid-attenuated inversion recovery; FOV: field of view; HASTE: half Fourier acquisition single shot turbo spin echo; H.E.: Hematoxylin-Eosin; IDIF: inferior vena cava; k_1: primary tracer uptake rate from blood to free tracer in tissue; k_2: tissue clearance rate; k_3: rates of exchange between free and trapped tracers in tissue; K_i: composite rate constant; k_{pl}: rate constant for pyruvate-lactate-exchange; $k_{pl,slice}$: rate constant for pyruvate-lactate-exchange measured in the whole CSI slice; MAT-B-III: mammary breast cancer cells derived from adenocarcinoma; MPRAGE: magnetization prepared rapid acquisition gradient echo; MRGLU: metabolic rate of glucose; MRAC: magnetic resonance-based attenuation correction; MR: magnetic resonance; MRI: magnetic resonance imaging; MRSI: magnetic resonance spectroscopic imaging; *p*: significance level; PET: positron emission tomography; *R*: Pearson correlation coefficient; ROI: region-of-interest; SUV_{max}: maximum standard uptake value; SUV_{mean}: mean of *SUV*s that are greater than SUV_{max} multiplied by a defined threshold (0.5 or 0.7) within a ROI; TAC: tumor uptake curve; T_1: spin-lattice relaxation time; T_2: spin-spin relaxation time; *TE*: echo time; *TLG*: total lesion glycolysis; *TMW*: tumor metabolic volume; *TR*: repetition time; UTE: ultra-short echo time; %-Nec.: mean of percentage of necrosis of analyzed histological slices.

References

1. Thackeray JT, Bankstahl JP, Bengel FM. Impact of image-derived input function and fit time intervals on Patlak quantification of myocardial glucose uptake in mice. J Nucl Med. 2015; 56: 1615-21.
2. Patlak CS, Blasberg RG, Fenstermacher JD. Graphical evaluation of blood-to-brain transfer constants from multiple-time uptake data. J Cereb Blood Flow Metab. 1983; 3: 1-7.
3. Phelps ME, Huang SC, Hoffman EJ, Selin C, Sokoloff L, Kuhl DE. Tomographic measurement of local cerebral glucose metabolic rate in humans with (^{18}F)2-fluoro-2-deoxy-D-glucose: validation of method. Ann Neurol. 1979; 6: 371-88.
4. Doblas S, Almeida GS, Ble FX, Garteiser P, Hoff BA, McIntyre DJ, et al. Apparent diffusion coefficient is highly reproducible on preclinical imaging systems: evidence from a seven-center multivendor study. J Magn Reson Imaging. 2015; 42: 1759-64.
5. Holz M, Heil SR, Sacco A. Temperature-dependent self-diffusion coefficients of water and six selected molecular liquids for calibration in accurate ^{1}H NMR PFG measurements. Phys Chem Chem Phys. 2000; 2: 4740-2.